

See discussions, stats, and author profiles for this publication at: <https://www.researchgate.net/publication/231641346>

Plasmonic Properties of Anchored Nanoparticles Fabricated by Reactive Ion Etching and Nanosphere Lithography

ARTICLE *in* THE JOURNAL OF PHYSICAL CHEMISTRY C · FEBRUARY 2007

Impact Factor: 4.77 · DOI: 10.1021/jp064094w

CITATIONS

50

READS

22

6 AUTHORS, INCLUDING:



[W. Paige Hall](#)

Pacific University Oregon

12 PUBLICATIONS 3,247 CITATIONS

SEE PROFILE

Plasmonic Properties of Anchored Nanoparticles Fabricated by Reactive Ion Etching and Nanosphere Lithography

Erin M. Hicks,[†] Olga Lyandres,[‡] W. Paige Hall,[†] Shengli Zou,[§] Matthew R. Glucksberg,[‡] and Richard P. Van Duyne^{*,†}

Department of Chemistry, Northwestern University, 2145 Sheridan Rd, Evanston, Illinois 60208-3113, Biomedical Engineering Department, Northwestern University, 2145 Sheridan Rd, Evanston, Illinois 60208-3113, and Chemistry Department, University of Central Florida, 4000 Central Florida Blvd, Orlando, Florida 32816-2366

Received: June 29, 2006; In Final Form: January 10, 2007

Aqueous environments pose unique challenges to the use of nanoparticle platforms for development of robust in vitro and in vivo sensors. A method is developed to anchor nanoparticles into a glass substrate by combining nanosphere lithography (NSL) and reactive ion etching (RIE) to create a mechanically durable sensing platform. The increased mechanical performance is attributed to the higher adhesion strength of NSL nanoparticles anchored in shallow nanowells formed by RIE. Using atomic force microscopy (AFM), anchored and conventional NSL nanoparticle arrays were subjected to increasing normal forces. The anchored nanoparticles were able to withstand normal forces 3 times greater (35.1 nN) compared to the conventional NSL nanoparticles (12.4 nN) prior to separation from the glass substrate. Superior adhesion in a constant flow aqueous environment is demonstrated by extinction measurements. After 1 h of 1.5 mL/min flow, extinction intensity decreased by 53% for bare and 13% for functionalized nanoparticles that were not anchored while extinction intensity decreased by only 15% for bare and less than 1% for functionalized nanoparticles that were anchored. A systematic shift to longer wavelengths is observed in the localized surface plasmon resonance (LSPR) spectra of the nanoparticle arrays as the embedded depth increases. This systematic shifting behavior of the LSPR wavelength maximum, λ_{max} , in the range from 678 to 982 nm, can be used to tune the plasmon position. LSPR shifting is used to demonstrate the detection of Alzheimer's precursor ligands as a potential biosensing application of the anchored nanoparticle arrays. Furthermore, we estimate the enhancement factors for SERS of the anchored nanoparticles are on the same order of magnitude (10^8) as the nanoparticles on flat substrates. Theoretical modeling is conducted to understand the shifting behavior of the anchored nanoparticle arrays.

Introduction

Fundamental properties, fabrication, and utilization of metal nanostructures have been at the forefront of the research community in the past decade. Arrays of metal nanoparticles, which have high extinction and scattering coefficients, are important for sensitive chemical and biological detection and the development of robust microelectronic devices.^{1,2} Nanosphere lithography (NSL) is one technique offering a versatile platform to examine the properties and explore the applications of such nanoparticle structures. NSL is a parallel, inexpensive fabrication method that produces, with a high degree of reproducibility and control, periodic nanoparticle arrays with adjustable size, shape, and material properties.^{3–5} NSL uses ordered arrays of hexagonally close-packed nanospheres as lithographic masks on silica, mica, silicon, and other solid surfaces. Typically, a thin layer of metal is deposited over the nanosphere mask. When the nanosphere mask is removed, an ordered array of metal nanoparticles remains on the surface. Several groups have combined NSL with thermal annealing^{6–8} and reactive ion etching (RIE)^{5,9} to expand the scope of NSL

by varying the shape and spacing of the metal nanoparticles. NSL has been widely used to examine optical properties of metal nanostructures,^{7,8,10–14} as well as to fabricate magnetic nanoparticles^{15–17} and photonic crystals.^{8,18} Furthermore, NSL-fabricated substrates have been used in biochemistry for protein nanoarrays¹⁹ and as sensors^{20–23} for various analytes.

This paper reports the use of NSL and RIE to fabricate embedded Ag nanoparticle arrays with improved adhesion and optical tuning. These robust structures can be employed in a variety of important applications including chemical and biological sensing. Etching is used at low power to selectively etch the SiO₂ substrate with a polystyrene nanosphere mask. The resulting structure is an array of triangular nanowells beneath the mask.⁵ After subsequent metal deposition, a portion of the nanoparticle is embedded in the substrate, thus anchoring it into the surface (Figure 1). While nanoparticle arrays on flat surfaces are structurally robust and stable in organic solvents, exposure to aqueous solutions (as is any biological milieu) significantly hinders their adhesion of metal to glass. The lattice mismatch between glass and silver forms an interface with a low strength of adhesion. In fact, this allows lift-off and separation of nanoparticles for applications such as tip fabrication.²⁴ Utilizing adhesion layers such as Ti and Cr^{20,25} is appropriate in surface plasmon resonance (SPR) measurements, where the metal film is continuous and the analyte does not

* To whom correspondence should be addressed. E-mail: vanduyne@chem.northwestern.edu.

[†] Department of Chemistry, Northwestern University.

[‡] Biomedical Engineering Department, Northwestern University.

[§] Chemistry Department, University of Central Florida.

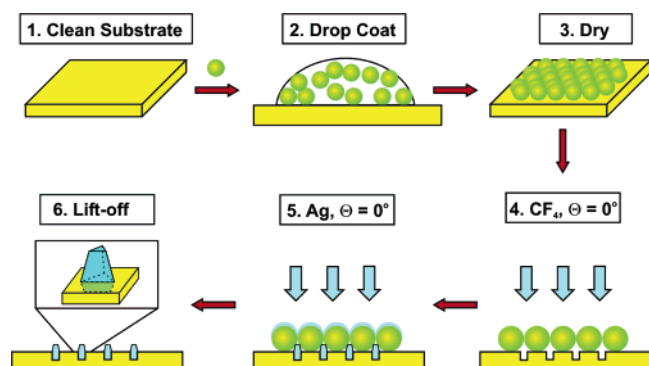


Figure 1. Schematic representation of the anchored nanoparticle array fabrication.

interact with the adhesion layer. However, in the case of nanoparticle arrays, exposed adhesion layers can cause non-specific binding and optical interference.²⁶ Anchoring the nanoparticles in the substrate offers a new and unique method to improve adhesion of metal nanoparticles to the surface without utilizing additional adhesion layers or specialized surfaces like mica. This method provides a universal platform that can be used for chemical and biological sensing applications without loss of regular nanoparticle array properties and advantages.

A key feature in the ability of the metal nanoparticle arrays to be used as sensors lies in the unique optical properties of the nanoparticles, called the localized surface plasmon resonance (LSPR). LSPR occurs when a specific wavelength of light impinges on the metallic nanoparticles, producing a collective oscillation of the conduction band electrons. This collective oscillation of electrons occurs only for light within a certain bandwidth; thus, metal nanoparticles exhibit selective photon absorption and resonant Rayleigh scattering, which can easily be monitored using UV–visible extinction spectroscopy. It is well-established that the maximum extinction wavelength, λ_{max} , of the LSPR is strongly and systematically dependent upon the composition, size, shape, and interparticle spacing of nanoparticles.^{4,7,13,14} The LSPR of the metal nanoparticle array can be exploited in two ways to achieve sensing: (1) by monitoring shifts in the LSPR extinction λ_{max} due to changes in the local dielectric environment; (2) by enhancing the electromagnetic field at the surface and thus enhancing Raman scattering of molecules adsorbed to the surface by factors as large as 10^{14} .^{27,28}

Superior adhesion of the anchored nanoparticles is evaluated by applying normal forces to the nanoparticles with an atomic force microscope (AFM) and subjecting the structures to constant flow conditions. Furthermore, a systematic study of the optical properties of anchored nanoparticles is conducted for a fixed nanoparticle height of 55 nm, while varying the depth of the nanowell. Herein we demonstrate control over the LSPR λ_{max} position in the wavelength range of ~ 300 nm (678–982 nm) for the use in the development of novel sensing modalities. As an example, we demonstrate the detection of Alzheimer's precursor ligands by monitoring the LSPR shifts, validating the potential use of anchored nanoparticles as a robust sensing platform. In addition, we show that the SERS enhancement factors from anchored nanoparticle surfaces are on the same order of magnitude as the nonanchored nanoparticle arrays. Discrete dipole calculations for the nanoparticles at various depths are conducted to elucidate the shifting behavior of the LSPR of the anchored nanoparticles. This work advances the capabilities, beyond conventional NSL methods, of nanoparticle systems in aqueous environments, where nanoparticle adhesion has traditionally been a challenge.

Experimental Section

Materials. Absolute ethanol was purchased from Pharmco (Brookfield, CT). Ag pellets (99.99%, 0.125 in diameter) were obtained from Kurt J. Lesker (Pittsburgh, PA). Borosilicate glass surfaces, No. 2 Fisherbrand 18-mm circle coverslips, were purchased from Fisher Scientific (Pittsburgh, PA). Polystyrene nanospheres with a diameter, D , of 500 ± 6 nm were received as a suspension in water. The nanosphere solutions were purchased from Interfacial Dynamics Corp. (Portland, OR). Millipore cartridges (Marlborough, MA) were used to purify water to a resistivity of $18 \text{ M}\Omega \text{ cm}^{-1}$. 1-octanethiol, benzenethiol, 11-mercaptopundecanoic acid (11-MUA), and phosphate buffered saline (PBS; pH = 7.4) were all purchased from Sigma-Aldrich (Milwaukee, WI). 1-Ethyl-3-(3-dimethyl-1-aminopropyl)carbodiimide hydrochloride (EDC) was purchased from Pierce (Rockford, IL). Amyloid derived diffusible ligands (ADDLs) and 20C2 were obtained from the Klein laboratory at Northwestern University. All materials were used without further purification.

Surface Preparation. The glass surfaces were cleaned in a piranha solution (1:3 30% H_2O_2 – H_2SO_4) at 80°C for 30 min. (**Caution:** *piranha solution should be handled with great care!*). Once cooled, the glass surfaces were rinsed with copious amounts of water and then sonicated for 60 min in 5:1:1 H_2O – NH_4OH –30% H_2O_2 . Last, the glass was rinsed repeatedly with water and stored in water until use. Single-layer colloidal crystal nanosphere masks were prepared by drop coating the nanosphere solution onto glass surfaces. Once the nanosphere masks were assembled, the surfaces were placed in a reactive ion etcher (RIE2000, South Bay Technology, Inc., San Clemente, CA) and etched for varying times with CF_4 gas. The samples were then mounted in an electron beam deposition system (Axxis Thin Film Electron Beam Evaporator, Kurt J. Lesker, Pittsburgh, PA). A metal thickness, d_m , of 55 nm of Ag was deposited at a rate of $\sim 0.3 \text{ \AA/s}$ on all samples used in the study. After the deposition, the nanospheres were removed by sonication in ethanol for 5 min. Atomic force micrographs for the three different surfaces are shown in Figure 2: a regular nanoparticle array; the nanowell surface; an anchored nanoparticle array.

LSPR Spectroscopy. Extinction spectroscopy measurements were carried out using a SD2000 spectrometer in transmission geometry coupled to a fiber probe (Ocean Optics, Dunedin, FL) and a halogen lamp (F-O-Lite H, World Precision Instruments, Sarasota, FL). The optimal wavelength range for this system is 400–950 nm.

Atomic Force Microscopy (AFM). AFM images were collected using a Digital Instruments Nanoscope IV AFM and Nanoscope IIIa controller operating in tapping mode, with etched Si nanoprobe tips (TESP, Digital Instruments, Santa Barbara, CA). The resonance frequencies of the cantilevers are between 280 and 320 kHz. The tips are conical in shape with a cone angle of 20° and an effective radius of curvature at the tip of 10 nm.

Mechanical Stability Study. A Digital Instruments Nanoscope IV AFM in contact mode with etched silicon tips (spring constant, 0.187 N/m) was used to study the stability of both the standard nanoparticle array and the anchored nanoparticle array. The sensitivity of the detector used for these experiments was 0.833 nm/V. Calibration of the AFM tips was performed on a clean glass slide. Normal force was applied at deflection setpoints of 0–5.75 V to produce a force calibration plot.

Solution Stability. Stability in aqueous environment under constant flow rate was assessed for bare and self-assembled monolayer (SAM) functionalized nanoparticles. Anchored nano-

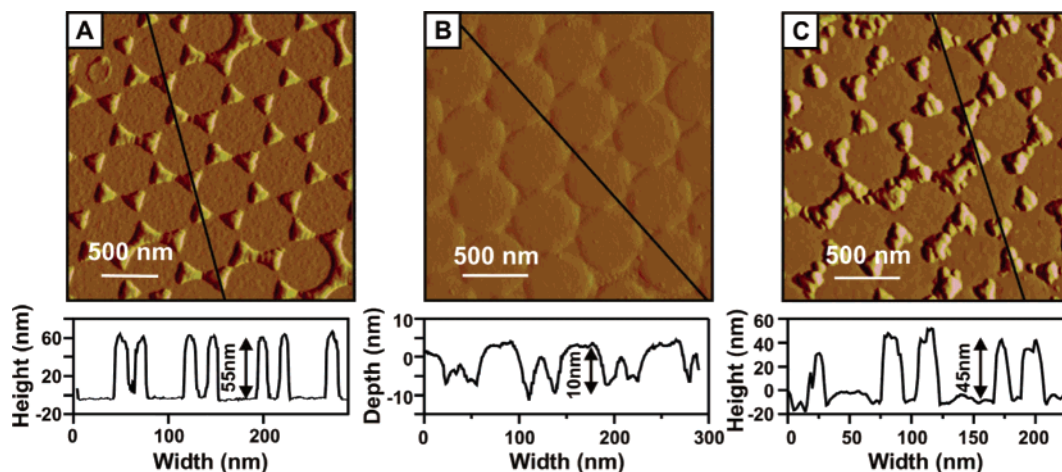


Figure 2. (A) AFM micrograph of a nanoparticle array on a flat surface with metal mass thickness, $d_m = 55$ nm. (B) AFM micrograph of fabricated nanowells, with no Ag deposited and nanowell depth ~ 10 nm. (C) AFM micrograph of particles in nanowells with 55 nm of Ag deposited onto the nanowell array resulting in an overall particle height of ~ 45 nm. All arrays were fabricated using a $D = 510$ nm nanosphere mask.

particle arrays were fabricated by etching for 3 min such that nanoparticles were anchored 6.6 nm into the surface. SAMs were utilized since they are commonly used to bind target analytes in the SPR and LSPR biosensors.^{20,25,29–33} The surfaces were incubated in a 3:1 solution of octanethiol and 11-MUA for 24 h. Both functionalized and nonfunctionalized nanoparticle arrays were then subjected to a constant flow of PBS. An automated syringe pump (New Era Pump Systems, Inc., Farmingdale, NY) was programmed to inject and withdraw fluid at a constant rate of 1.5 mL/min. The samples were exposed to the flowing environment for 1 h. LSPR spectra were collected in N_2 before the flow was turned on and after being subjected to constant flow for 1 h.

ADDLs Detection. Anchored nanoparticle samples were fabricated by etching for 3 min, anchoring the nanoparticles 6.6 nm into the surface. These samples were then incubated overnight in a 9:1 solution of octanethiol and 11-MUA. Prior to the initial spectrum, the samples were rinsed in ethanol and dried in nitrogen. A mixture of 500 nM ADDLs and 1 mM EDC solutions was then injected into the flow cell and allowed to incubate for 1 h. The sample was then rinsed with PBS and pH balanced water and dried in nitrogen for spectrum collection. Finally, a 100 nM solution of the anti-ADDLs antibody 20C2 was injected and allowed to bind to the ADDLs. After a 30 min incubation, the sample was again rinsed with PBS and pH-balanced water and dried in nitrogen for final spectrum collection.

Surface-Enhanced Raman Spectroscopy. All optical measurements were performed using a Nikon Eclipse TE300 inverted microscope (Fryer Co., Huntley, IL) equipped with a 20 \times objective (NA = 0.5). Substrates were mounted on a piezoelectric stage (model P-517.3CD, Polytech PI, Auburn, MA) to allow for sample positioning and raster-scanning during spectral acquisition. The light scattered by the samples was analyzed with a TriplePro three-stage spectrograph equipped with a liquid-nitrogen-cooled, deep-depletion Spec-10:400BRCCD detector (Roper Scientific, Trenton, NJ). A color video camera was also attached to the front port of the microscope to facilitate laser alignment and positioning of the samples. Laser excitation was provided by the Spectra-Physics (Mountain View, CA) Millennia Xs ($\lambda_{ex} = 532$ nm) and a Spectra-Physics Tsunami with GWU harmonic generator ($\lambda_{ex} = 350–500, 700–1000$ nm). The laser light from the tunable laser systems was filtered using Pellin-Broca prisms or a diffraction grating to ensure monochromatic illumination of the

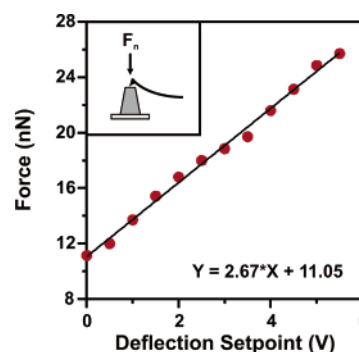


Figure 3. Normal force applied by the AFM cantilever as a function of deflection setpoint on a clean glass surface. The setpoint was varied between 0 and 5.75 V, and the corresponding force was calculated. The linear regression fit allows calculation of the force applied to the particles at setpoints outside the 0–5.75 range. The inset shows a schematic of the force applied by the cantilever.

sample. For the NSL-fabricated triangular nanoparticles, in-situ measurement of the LSPR spectrum was achieved by illuminating the sample with the microscope lamp and analyzing the transmitted light with a fiber-optically coupled miniature spectrometer (model SD2000, Ocean Optics, Dunedin, FL).

Results and Discussion

Nanoparticle Adhesion. Anchored nanoparticles provide a more robust, mechanically stable substrate for sensor applications. Adhesion of the nanoparticles to the surface was examined by the AFM normal force measurements. Normal force applied by the AFM cantilever can be calculated by

$$F_n = k(DS)z$$

where k is the spring constant of the cantilever measured in N/m, DS is the detector sensitivity reported in the units of nm/V, and z is the deflection of the cantilever given in V. The force calibration plot is shown in Figure 3. The linear fit to the data allows the calculation of forces applied to the samples outside of the calibration range.³⁴

Normal force, although not a direct measure of adhesion, gives a relative qualitative characteristic of the nanoparticles' stability. It is the vertical component of the force applied by the cantilever as it scans the surface of the substrate (Figure 3 inset). The normal force needed to remove metal nanoparticles from an unetched glass surface was determined for comparison.

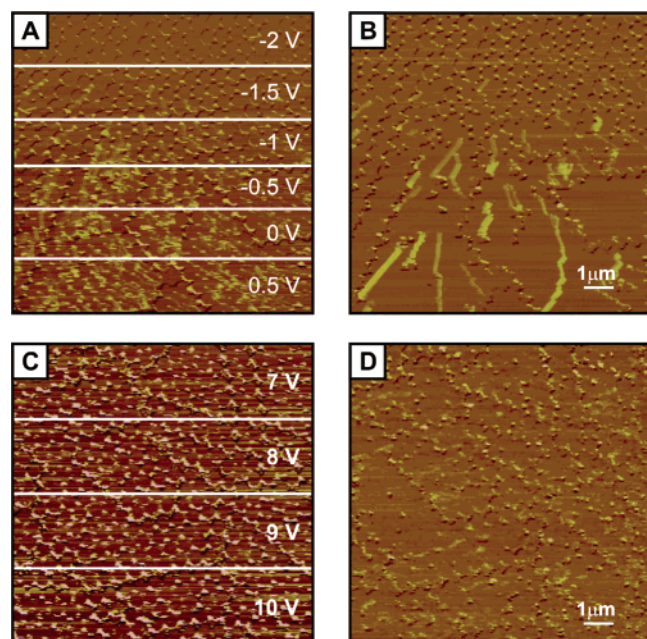


Figure 4. (A) Contact AFM image of nanoparticles on a glass substrate with increasing setpoint during the scan. At -1.5 V (7.05 nN), the nanoparticles just begin to move, and at 0.5 V (12.39 nN), most particles have moved. (B) Contact AFM image of the same area at a fixed low setpoint of -2 V. Most nanoparticles in the bottom section have been removed, and more nanoparticles shifted as a low force was applied to them in the consecutive scan. (C) Contact AFM image of anchored particles on a glass substrate with increasing setpoint during the scan. At 5 V (24.4 nN), the particles just begin to move (data not shown), and at 9 V (35.08 nN), most particles have moved. (D) Contact AFM image of the same area at a fixed low setpoint of 1 V. Most particles in the bottom section have been removed, and more nanoparticles shifted as a low force was applied to them in the consecutive scan.

The nanoparticles were fabricated using a 510 nm nanosphere mask. The resulting particles had an out-of-plane height of 55 nm Ag. A $100 \mu\text{m}^2$ area of the substrate was scanned using contact mode AFM with an incrementally increasing deflection setpoint (Figure 4A) from -2 to 0.5 V. The nanoparticles began

to be displaced from the surface at -1.5 V, a setpoint corresponding to a normal force of 7.05 nN. Moving nanoparticles are characterized on the image by the trail left behind after being dragged by the tip. Most of the nanoparticles were removed at a setpoint of 0.5 V, which is equivalent to a normal force of 12.39 nN. A second scan of the same area was acquired at a low deflection setpoint of -2 V to view the resulting structure (Figure 4B). The metal structures formed from line defects in the nanosphere mask remain on the surface. Several nanoparticles appear to be displaced even at this low setpoint due to the stress applied by the cantilever in the previous scan. The normal force calculated agrees with previously reported normal force measurements needed to displace metal nanoparticles.^{25,35}

Anchored nanoparticle substrates were examined in the same manner. The anchored nanoparticles were fabricated using a 510 nm sphere mask with a 3 min etch at 25 W, and 55 nm of Ag was deposited. The nanoparticles were embedded into a well 10 – 15 nm deep. Contact force AFM scans over a $100 \mu\text{m}^2$ area were acquired with incrementally increasing deflection setpoints. For each deflection range, a new area was scanned to maintain uniform conditions. The anchored nanoparticles were not displaced with deflection setpoints between -2 and 4 V. They began to move with a deflection setpoint of 5 V (24.4 nN (data not shown)). Most of the nanoparticles were removed at a deflection setpoint of 9 V (35.08 nN (Figure 4C)). Another image of the same area was acquired at a low deflection setpoint of 1 V to view the resulting structure (Figure 4D). The metal structures formed from line defects in the nanosphere mask remain on the surface. These results indicate that the anchored nanoparticles provide a more robust surface for sensors than nanoparticle arrays on flat glass substrate. Anchoring the nanoparticles results in a 3-fold improvement in mechanical stability of the structure. This increase in mechanical stability allows the anchored nanoparticle arrays to be placed in harsh environments where traditional arrays would become damaged or delaminated.

Solution Stability of Nanoparticle Arrays. Mechanical stability of anchored and nonanchored nanoparticle arrays was

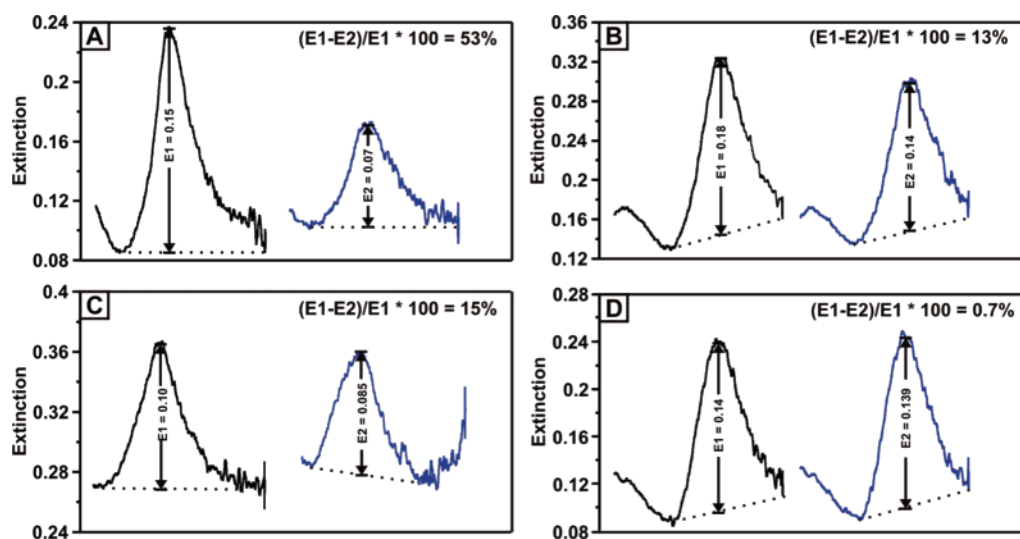


Figure 5. Solution stability of nonanchored and anchored nanoparticle arrays with and without the SAM as evaluated by changes in extinction intensity: (A) a nonanchored nanoparticle array with no SAM results in a 53% decrease in extinction intensity; (B) SAM-functionalized anchored nanoparticle array results in a 13% drop in intensity; (C) an anchored nanoparticle array with no SAM exhibits only a 15% decrease in intensity; (D) SAM-functionalized anchored nanoparticle array results in a less than 1% change in extinction intensity. For all samples, the metal mass thickness, $d_m = 55$ nm. All samples were exposed to a constant flow rate of 1.5 mL/min by an automated syringe pump that pushed and withdrew pH-balanced water for a total of 1 h. In all graphs, the initial LSPR spectra in N_2 are shown in black and the spectra following the 1 h exposure to fluid flow dried and acquired in N_2 are shown in blue.

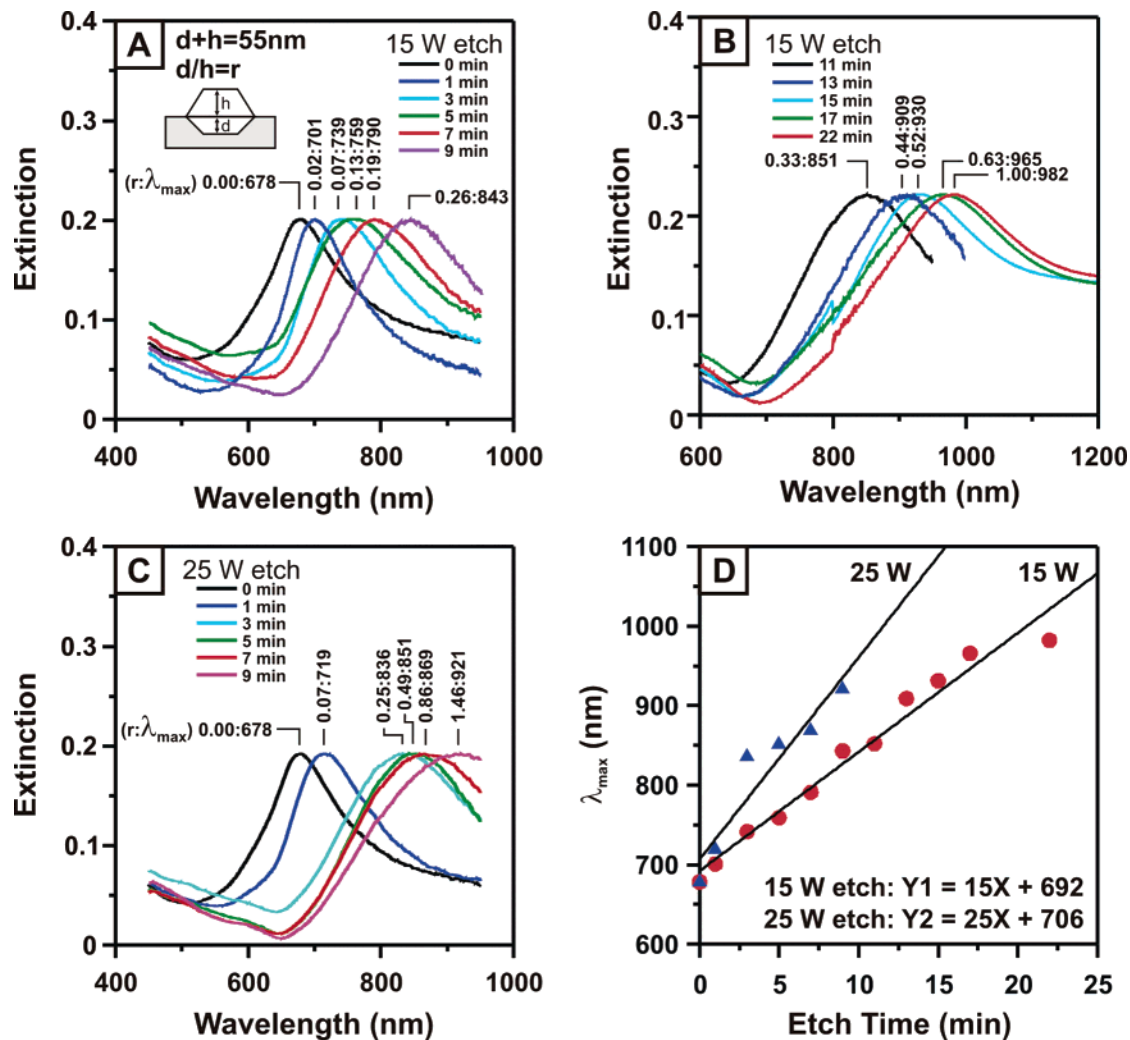


Figure 6. LSPR extinction spectra of anchored nanoparticles on glass substrates for different etch times and etch power. As the etch time increases, the depth of the well increases, making the metal nanoparticles more embedded in the glass. A corresponding LSPR red shift is observed with increasing etch time. LSPR spectra are shown for 15 W etch for (A) 0–9 min etch and (B) 11–22 min etch. (C) LSPR spectra are shown for 25 W etch for 0–9 min etch. (D) The linear shift in LSPR λ_{max} is observed as a function of etch time. For the fitted trend lines, $R^2_{15} = 0.97$ and $R^2_{25} = 0.90$ for the 15 and 25 W etch, respectively. CF_4 etch: pressure = 10 mTorr; $D = 500$ nm; $d_m = 55$ nm; deposition rate = 0.4 \AA/s .

TABLE 1: Embedded Particle Arrays and Corresponding Properties^a

etch time (min)	etch depth ^b	out-of-plane particle height ^b	plasmon λ_{max} ^b
0	0	55	678
1	2.57	52.43	701
3	6.57	48.43	739
5	8.77	46.23	759
7	12.67	42.33	790
9	14.96	40.04	843
11	18.07	36.93	851
13	20.62	34.38	909
15	24.27	30.73	930
17	27.37	27.63	965
22	35.12	19.88	982

^a For all particles, the following parameters: etch power, $P = 15$ W; sphere mask diameter, $D = 500$ nm; material, Ag; Ag mass thickness, $d_m = 55$ nm. ^b Measurements in nm.

further examined by subjecting the substrates to flow conditions for an extended period of time similar to the biosensing assays involving incubation and rinsing steps. Both bare and SAM-functionalized nanoparticle arrays were examined. Figure 5 details a study performed on 4 different samples: (1) non-anchored bare nanoparticles; (2) nonanchored nanoparticles with SAM; (3) anchored bare nanoparticles; (4) anchored nanopar-

ticles with SAM. Extinction spectra before and after the rigorous flowing environment were collected to assess the extinction efficiency of the substrate, which corresponds to the number of nanoparticles that can scatter and absorb the incident light. The most dramatic effect can be seen in the samples fabricated on a flat surface (Figure 5A,B). In Figure 5A, it is evident that a large number of nanoparticles have come off the surface. This is illustrated by a 53% drop in the extinction intensity. Functionalizing the nanoparticles with a SAM helps to stabilize the nanoparticles, yet there is still a 13% decrease in extinction intensity. The bare anchored nanoparticles (Figure 5C) are significantly more stable in solution as there is only a 15% decrease in the LSPR intensity of the nanoparticle array under the same constant flow conditions. The extinction from the SAM-functionalized anchored nanoparticles does not decrease in intensity, showing that, with a SAM as a protective layer, the nanoparticles are completely stable in an aqueous environment. This makes the anchored nanoparticle arrays an ideal platform for the engineering of LSPR chemo- and biosensors.

Optical Properties of the Anchored Nanoparticles. The optical properties of the anchored nanoparticle arrays produced by NSL and RIE were examined as a function of varying nanowell depth. The power used in the etching process is directly proportional to the etch rate of the material. Thus, at

higher powers, etching occurs faster and can adversely affect the integrity of the polystyrene nanosphere mask. Polystyrene undergoes etching at a much slower rate than silicon. However, the nanospheres are visibly affected as the power and time of the etch are increased. Rather than forming an array of discrete nanoparticles, at high powers the process results in a continuous metallic network, which does not produce a well-defined LSPR band. The connection of the nanowells is a byproduct of the shrinking nanosphere mask (caused by etching of the nanospheres). Slower etch rates result in more uniform nanowells, even for longer etch times.

The etch time controls the depth of the nanowells and thus how deeply the nanoparticles are embedded into the substrate. The etch times ranged from 1 to 25 min and from 1 to 9 min for the 15 and 25 W power etches, respectively. Table 1 summarizes well depth and out-of-plane nanoparticle height, as well as the LSPR maximum wavelength, λ_{max} , for the substrates etched with 15 W. The LSPR λ_{max} shifts red as the depth of the nanowell increases (Figure 6). This systematic shifting is explained by the fact that glass has a higher refractive index than air ($\text{RI}_{\text{glass}} = 1.5$, $\text{RI}_{\text{air}} = 1.0$). As the nanoparticles are embedded further into the glass substrate, more of the nanoparticle interacts with the higher refractive index material, thus red shifting the LSPR λ_{max} . This feature provides a method to tune the LSPR peak position by controlling the depth of the nanowell in addition to the size of the nanoparticle and its out-of-plane height. The broadening of the LSPR bands can be attributed to the merging of the nanoparticles as the polystyrene mask is etched away with the increasing etch times. For 15 W etches (Figure 6A,B), the continuous network is formed after 25 min of etching (LSPR spectrum not shown). In the case of the 25 W etches (Figure 6C), the LSPR range is more limited since the nanoparticles merge faster, and no LSPR spectra were obtained for etches longer than 9 min. Both sets of data show linear relationship between λ_{max} position as a function of etch time (Figure 6D).

LSPR Biosensing Platform. We have carried out an initial biosensing experiment to demonstrate the detection of ADDLs, an Alzheimer's precursor, as shown in Figure 7A. A depiction of the binding events being probed is also shown in Figure 7B. First, the nanoparticles are functionalized with the SAM, such that the LSPR $\lambda_{\text{max}} = 825.8$ nm. When ADDLs are injected, they covalently bind to the SAM via an EDC-catalyzed reaction and cause the λ_{max} to red shift to 836.8 nm. The shift of 11 nm is due to the increase in the refractive index around the nanoparticles. Binding of the 20C2 antibody to the ADDLs results in an additional red shift of 8 nm with the final LSPR $\lambda_{\text{max}} = 844.8$ nm. As can be seen in Figure 7A, anchoring the nanoparticles only 6.6 nm into the surface keeps them very stable throughout the incubation and rinsing procedure with no decrease in plasmon intensity as the experiment continues (data not shown). Furthermore, the shifts seen in the plasmon resonance are typical for this type of experiment.²⁰ With no decrease in plasmon intensity and the same sensitivity, the anchored nanoparticle systems successfully illustrate their viability as a new platform for fabricating LSPR chemo- and biosensors.

SERS Sensing Platform. Benzenethiol was used as a probe molecule to test the potential of the anchored nanoparticles for use as a SERS-active substrate. SERS signal intensities on anchored nanoparticle arrays and nonanchored nanoparticle arrays were compared to access the enhancement capabilities. Benzenethiol was chosen due to its large Raman cross section and ease of binding to the Ag surface. The substrates were

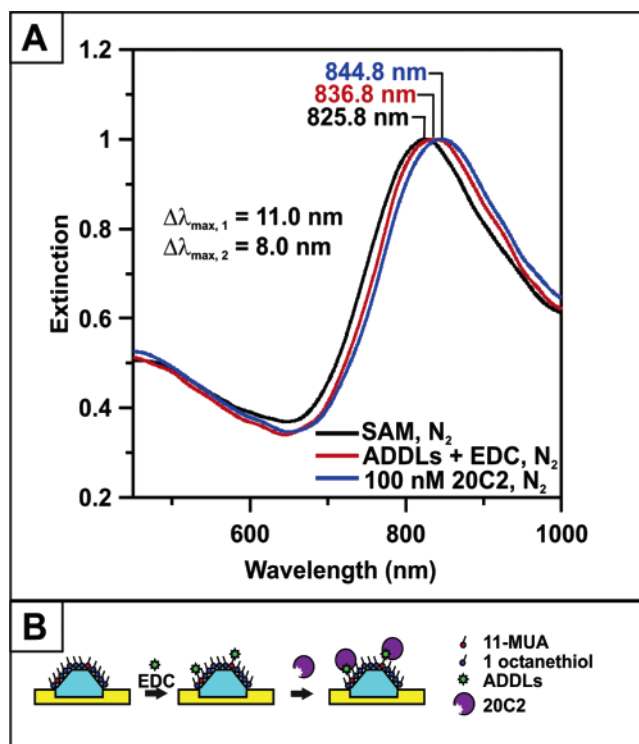


Figure 7. Detection of ADDLs using anchored nanoparticles. The SAM-functionalized anchored nanoparticle array has an LSPR λ_{max} of 825.8 nm. With the addition of ADDLs and EDC, the plasmon red shifts 11 nm to 836.8 nm. The second red shift of 8 nm is observed upon the addition of 20C2 antibody.

functionalized with a benzenethiol SAM, and SER spectra were acquired at an optimal excitation wavelength to maximize the enhancement (Figure 8). The optimal wavelengths were determined by the LSPR λ_{max} of the nanoparticle arrays, which are shown in the insets in Figure 8A,B for the nonanchored and anchored nanoparticles, respectively. The optimal wavelength needs to be blue-shifted from the LSPR λ_{max} such that the average of excitation wavelength and the scattered photon wavelength is equal to LSPR λ_{max} .³⁶ Optimal excitation wavelength for nonanchored nanoparticles was determined to be 750 nm, and that for the anchored nanoparticles, 718 nm. The spectra of benzenethiol were scaled with respect to the normal Raman spectra of cyclohexane at both wavelengths to correct for detection system efficiency, power, and ν^4 dependence in Raman scattering. The intensity of the 1000 cm^{-1} band was analyzed to assess the Raman enhancement from the nanoparticle arrays. The intensity of the band on nonanchored nanoparticles is 1.6 while the intensity on anchored nanoparticles is 1.1, 31% lower. The enhancement factors for both substrates are the same order of magnitude, and only a slight decrease in intensity is observed. The decrease can be attributed to a decreased number of benzenethiol molecules binding to the nanoparticles since part of it is embedded into the glass substrate. Furthermore, fewer nanoparticles are probed, since the amplitude of the LSPR spectrum of the anchored nanoparticle array is slightly lower at the sampled spot than that of the nonanchored nanoparticle array.³⁷ In summary, anchored nanoparticles provide a robust sensing platform with enhancement factors comparable to the ones of nanoparticles on flat substrates but with superior mechanical and solution stability.

Theoretical Modeling. The systematic red-shifting of anchored nanoparticles is expected due to the fact that glass has a higher refractive index than that of air ($\text{RI}_{\text{glass}} = 1.5$, $\text{RI}_{\text{air}} = 1.0$). As the nanoparticles are embedded further into the glass

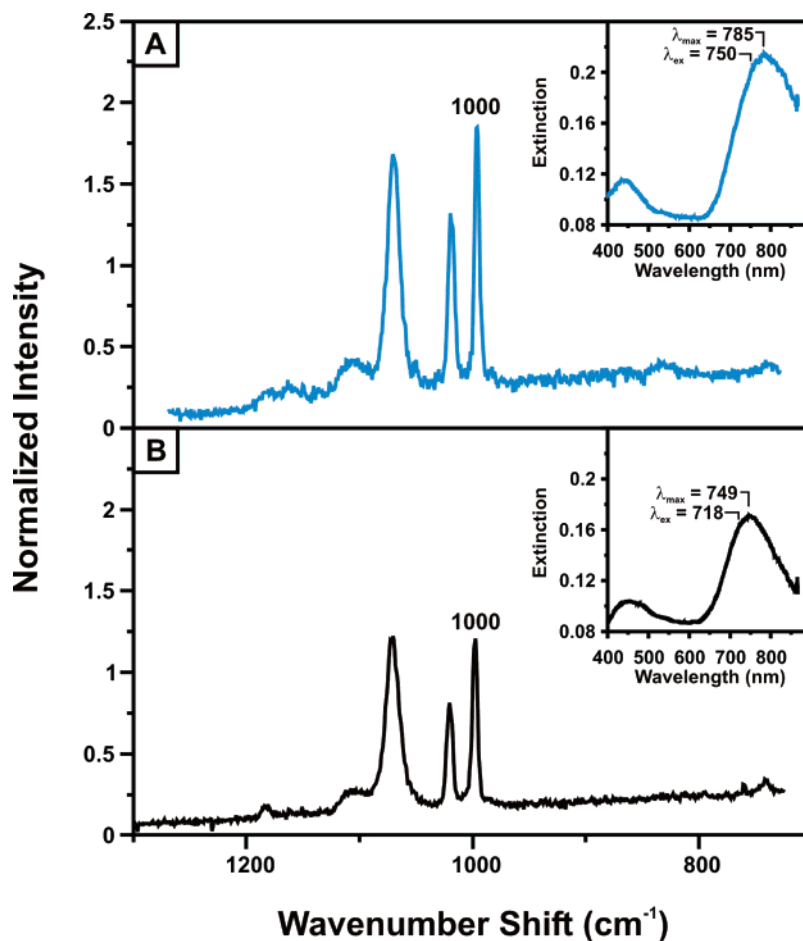


Figure 8. SERS spectra of benzenethiol on (A) nonanchored and (B) anchored nanoparticle arrays. Intensity is normalized with respect to normal Raman scattering intensity of cyclohexane at both wavelengths. The insets show corresponding extinction spectra for structures tested. The intensity of the 1000 cm⁻¹ band of benzenethiol is 1.6 for the nonanchored particles and 1.1 for the anchored particles: (A) λ_{ex} = 750 nm, P = 10 mW, t = 150 s, normalized intensity of 1 corresponds to 6600 counts; (B) λ_{ex} = 718 nm, P = 8.25 mW, t = 150 s, normalized intensity of 1 corresponds to 13 300 counts.

substrate, more of the nanoparticle interacts with the higher refractive index material, thus red shifting the LSPR λ_{max} . However, the 304 nm shift from 678 to 982 nm cannot be solely attributed to the change of the embedding depth of nanoparticles into the glass substrate. Previously, Malinsky et al.²² found that, for a nanoparticle with a bisector of 100 nm and height of 50 nm, the plasmon resonance shift is 150 nm when the refractive index of the environment changes by 1. That is far less than observed in the experiment.

The discrete dipole method³⁸ is applied to further understand the mechanism of the shifting. We first modeled a truncated tetrahedral silver nanoparticle with a bisector of 118 nm and height of 54 nm which is close to the geometry of the nanoparticle prepared in the experiments. The resonance wavelength of the nanoparticle is 565 nm in vacuum and 806 nm in glass ($RI = 1.52$). To simulate nanoparticles sitting on or embedded in glass substrate, we treat nanoparticles above the substrate as a truncated tetrahedron and the embedded part as a prism which has the same side length as the tetrahedron (Figure 9B,C). The total height (height of the embedded prism and exposed truncated tetrahedron) of the nanoparticle is always kept to be 54 nm to be consistent with the experiments. The effective medium theory was applied to the simulation to include the substrate effect. The plasmon resonance wavelength of the nanoparticle on a flat glass substrate is 643 nm, which is 35 nm shorter than the measured wavelength. When the nanoparticle is embedded into glass 30 nm, the calculated resonance

wavelength is 701 nm. The simulated extinction efficiency for embedded nanoparticles at various depths is shown in Figure 9B. The calculated shift is only 58 nm, which is significantly lower than the experimental observation of a 304 nm shift when the embedded depth increases from 0 to 30 nm.

This theoretical model does not take into account the changes in the shape of the nanoparticles as the well depth increases. Due to the fact that the polystyrene mask is etched away with the increasing etch time, the sides of the nanowells are tilted, thus the embedded part of the nanoparticle needs to be treated as an upside down truncated tetrahedron which has the same side length as the exposed one. As a result, the perpendicular bisector, a , of the nanoparticle increases with etch time, thus widening the nanoparticles. In the following simulations, we treat the embedded part of the nanoparticle as an inverted tetrahedron and increase the bisector of nanoparticles with the increase in nanowell depth (Figure 9E). The rate of widening is controlled so that when the embedded depth is 30 nm, the bisector of the nanoparticle is increased to 200 nm, which is close to the experimental record. We modeled an isolated single nanoparticle (Figure 9AI). When the nanoparticle is on a flat substrate, the resonance remains at 643 nm (data not shown). When the embedded depth is increased to 10 nm, the plasmon resonance wavelength red shifts to 711 nm, and when the embedded depth is increased to 30 nm, the resonance wavelength red shifts further to 899 nm. The calculated value is still almost 100 nm shorter compared to the experimental data.

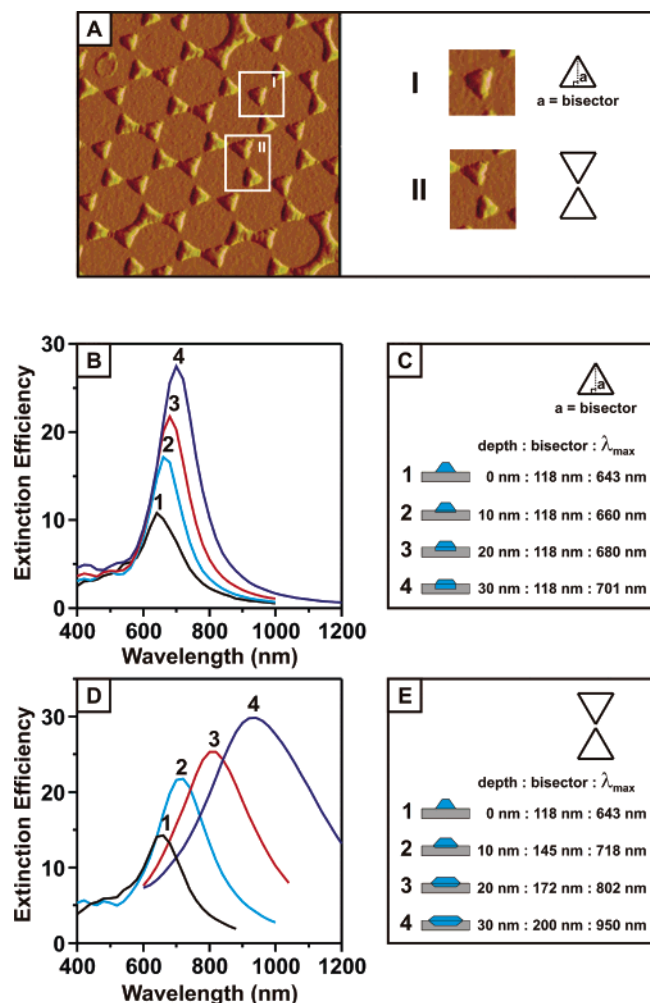


Figure 9. Discrete dipole simulation results with AFM images and schematics of the nanoparticles modeled (AI, AII). Initially, prism-shaped wells with increasing well depth are modeled (B, C). Particle height, b , and bisector, a , are kept constant at 54 and 118 nm, respectively. For a more accurate representation, dimers of particles with increasing bisector were modeled (D, E). Particle height is kept constant at 54 nm, while the bisector increases from 118 to 200 nm at the rate of 2.7 nm/nm of embedded depth.

In the above simulations, we consider only an isolated nanoparticle and the polarization of the incident light is taken to be parallel to one side of the truncated tetrahedron. To include the coupling between nanoparticles, we also modeled nanoparticle dimers in which two truncated tetrahedrons are arranged head to head as shown in Figure 9AII. When the polarization of the incident light is perpendicular to the symmetry axis, the resonance wavelength is close to that of an isolated nanoparticle. When the polarization is parallel to the symmetry axis, the strong coupling between nanoparticles pushes resonance wavelength further to the longer wavelengths when the distance between the nanoparticles is decreasing. The resonance wavelength of the dimer is 718 nm when the well depth is increased to 10 nm with the polarization of the light parallel to the symmetry axis. This shows that the coupling between nanoparticles is not strong when the embedded depth is less than 10 nm. When the embedded depth is increased to 30 nm, the resonance wavelength of the dimer with polarization of the incident wave parallel to the symmetry axis is at 1005 nm. Since the light in the experiments is not polarized, we averaged the resonance wavelengths from parallel and perpendicular polarizations and obtained the resonance wavelength of 950 nm, which agrees well with the experimental value of 982 nm. The simulated

extinction efficiency for dimers of nanoparticles with increasing bisector at various well depths is shown in Figure 9D,E.

Through the theoretical model, we learned that the red shifts of nanoparticle resonance wavelengths are due to the change in the index of refraction of the medium as well as the widening of the nanoparticle due to the etching of the polystyrene mask with the increasing etch time. The strong coupling between nanoparticles also plays an important role in the observed red shift with the increasing etch time. The broadening of the resonance peak can be interpreted by the widening of the nanoparticles, which results in a broader and red-shifted resonance peak. The increased discrepancy between plasmon resonance wavelengths for parallel and perpendicular polarized light when nanoparticles are getting closer also contributes to the broadening of the resonance peaks. The decrease in the uniformity of the nanoparticles may also be an important factor in broadening the resonance peak with increasing etch time.

Conclusion

In this paper, we have demonstrated the fabrication of mechanically robust and optically tunable substrates for chemical and biological sensing using nanosphere lithography and reactive ion etching. A 3-fold increase in adhesion was achieved by embedding the nanoparticles only 10–15 nm into the glass surface. Nanoparticle adhesion is further evaluated in an aqueous environment with constant flow, demonstrating superior adhesion for anchored nanoparticles. This dramatic increase in the stability of the nanoparticles will allow the use of these architectures in more rigorous environments (e.g., aqueous solutions) required for biological sensing. We successfully constructed a general platform with improved stability, while maintaining a structure with carefully controlled optical properties and electromagnetic field enhancements appropriate for sensing applications. Controlled tunability of the LSPR λ_{\max} has been achieved by varying the nanowell depth of the glass substrate. This tunability will allow for fine adjustments in the plasmon peak position of the nanoparticle arrays to maximize enhancements needed for high detection sensitivity. We demonstrated the feasibility of using the fabricated surfaces for LSPR measurements to detect Alzheimer's precursor ligands and show that enhancement factors for SERS are on the same order of magnitude as nanoparticle arrays on flat surfaces. Finally, theoretical calculations were conducted to elucidate the systematic shifting behavior of the LSPR of the anchored nanoparticles.

Acknowledgment. We gratefully acknowledge the support from the National Science Foundation (Grants CHE-0414554, DMR-0520513, EEC-0118025, BES-0507036), the National Institutes of Health (Grant 4 R33 DK066990-02), the Air Force Office of Scientific Research MURI program (Grant F49620-02-1-0381). We thank William L. Klein of the Department of Neurobiology and Physiology at Northwestern University for providing ADDLs and 20C2 antibodies for the LSPR sensing experiment. Also, we greatly appreciate the help of Jon Dieringer in acquiring the SERS data. In addition we acknowledge Dr. Chanda Yonzon, Ms. Nilam Shah, Dr. Douglas Stuart, and Dr. Katherine Willets at Northwestern University for helpful comments. E.M.H. and O.L. contributed equally to this work.

References and Notes

- (1) Choi, W. B.; Bae, E.; Kang, D.; Chae, S.; Cheong, B.; Ko, J.; Lee, E.; Park, W. *Nanotechnology* **2004**, *15*, S512.
- (2) Liang, Y.; Zhai, L.; Zhao, X.; Xu, D. *J. Phys. Chem. B* **2005**, *109*, 7120.

- (3) Hulteen, J. C.; Van Duyne, R. P. *J. Vac. Sci. Technol., A* **1995**, *13*, 1553.
- (4) Hulteen, J. C.; Treichel, D. A.; Smith, M. T.; Duval, M. L.; Jensen, T. R.; Van Duyne, R. P. *J. Phys. Chem. B* **1999**, *103*, 3854.
- (5) Whitney, A. V.; Myers, B. D.; Van Duyne, R. P. *Nano Lett.* **2004**, *4*, 1507.
- (6) Tan, B. J. Y.; Sow, C. H.; Koh, T. S.; Chin, K. C.; Wee, A. T. S.; Ong, C. K. *J. Phys. Chem. B* **2005**, *109*, 11100.
- (7) Jensen, T. R.; Duval, M. L.; Kelly, K. L.; Lazarides, A. A.; Schatz, G. C.; Van Duyne, R. P. *J. Phys. Chem. B* **1999**, *103*, 9846.
- (8) Kempa, K.; Kimball, B.; Rybczynski, J.; Huang, Z. P.; Wu, P. F.; Steeves, D.; Sennett, M.; Giersig, M.; Rao, D. V. G. L. N.; Carnahan, D. L.; Wang, D. Z.; Lao, J. Y.; Li, W. Z.; Ren, Z. F. *Nano Lett.* **2003**, *3*, 13.
- (9) Haynes, C. L.; Haes, A. J.; Van Duyne, R. P. *Mater. Res. Soc. Symp. Proc.* **2001**, *635*, C6 3/1.
- (10) Chung, J. K.; Onuta, T.; Schaich, W. L.; Dragnea, B. *Abstracts of Papers*, 230th National Meeting of the American Chemical Society, Washington, DC, Aug 28–Sept 1, 2005; American Chemical Society: Washington, DC, 2005; ANYL.
- (11) Haynes, C. L.; Van Duyne, R. P. *Nano Lett.* **2003**, *3*, 939.
- (12) Haynes, C. L.; Van Duyne, R. P. *J. Phys. Chem. B* **2001**, *105*, 5599.
- (13) Malinsky, M. D.; Kelly, K. L.; Schatz, G. C.; Van Duyne, R. P. *J. Phys. Chem. B* **2001**, *105*, 2343.
- (14) Jensen, T. R.; Malinsky, M. D.; Haynes, C. L.; van Duyne, R. P. *J. Phys. Chem. B* **2000**, *104*, 10549.
- (15) Weekes, S. M.; Ogrin, F. Y. *J. Appl. Phys.* **2005**, *97*, 10J503/1.
- (16) Rybczynski, J.; Hilgendorff, M.; Giersig, M. *NATO Sci. Ser., Ser. 2* **2003**, *91*, 163.
- (17) Weekes, S. M.; Ogrin, F. Y.; Murray, W. A. *Langmuir* **2004**, *20*, 11208.
- (18) Han, S.; Hao, Z.; Wang, J.; Luo, Y. *J. Vac. Sci. Technol., B* **2005**, *23*, 1585.
- (19) Cai, Y.; Ocko, B. M. *Langmuir* **2005**, *21*, 9274.
- (20) Haes, A. J.; Hall, W. P.; Chang, L.; Klein, W. L.; Van Duyne, R. P. *Nano Lett.* **2004**, *4*, 1029.
- (21) Yonzon, C. R.; Jeoung, E.; Zou, S.; Schatz, G. C.; Mrksich, M.; Van Duyne, R. P. *J. Am. Chem. Soc.* **2004**, *126*, 12669.
- (22) Malinsky, M. D.; Kelly, K. L.; Schatz, G. C.; Van Duyne, R. P. *J. Am. Chem. Soc.* **2001**, *123*, 1471.
- (23) Stranik, O.; McEvoy, H. M.; McDonagh, C.; MacCraith, B. D. *Sens. Actuators, B* **2005**, *B107*, 148.
- (24) Haes, A. J.; Zhao, J.; Zou, S. L.; Own, C. S.; Marks, L. D.; Schatz, G. C.; Van Duyne, R. P. *J. Phys. Chem. B* **2005**, *109*, 11158.
- (25) Riboh, J. C.; Haes, A. J.; McFarland, A. D.; Yonzon, C. R.; Van Duyne, R. P. *J. Phys. Chem. B* **2003**, *107*, 1772.
- (26) Haes, A. J.; Haynes, C. L.; McFarland, A. D.; Zou, S.; Schatz, G. C.; Van Duyne, R. P. *MRS Bull.* **2005**, *30*, 368.
- (27) Emory, S. N. a. S. R. *Science* **1997**, *275*, 1102.
- (28) Kneipp, K.; Kneipp, Y. W. H.; Perelman, L.T.; Itzkan, I.; Dasari, R. R. Feld, M. S. *Phys. Rev. Lett.* **1997**, *78*, 1667.
- (29) Haes, A. J.; Chang, L.; Klein, W. L.; Van Duyne, R. P. *J. Am. Chem. Soc.* **2005**, *127*, 2264.
- (30) Berger, C. E. H.; Beumer, T. A. M.; Kooyman, R. P. H.; Greve, J. *Anal. Chem.* **1998**, *70*, 703.
- (31) Brockman, J. M.; Frutos, A. G.; Corn, R. M. *J. Am. Chem. Soc.* **1999**, *121*, 8044.
- (32) Homola, J.; Yee, S. S.; Gaultz, G. *Sens. Actuators, B* **1999**, *54*, 3.
- (33) Houseman, B. T.; Mrksich, M. *Chem. Biol.* **2002**, *9*, 443.
- (34) Cleveland, J. P.; Manne, S.; Bocek, D.; Hansma, P. K. *Rev. Sci. Instrum.* **1993**, *64*, 403.
- (35) Eppler, A. S.; Rupprechter, G.; Anderson, E. A.; Somorjai, G. A. *J. Phys. Chem. B* **2000**, *104*, 7286.
- (36) McFarland, A. D.; Young, M. A.; Dieringer, J. A.; Van Duyne, R. P. *J. Phys. Chem. B* **2005**, *109*, 11279.
- (37) Haynes, C. L.; Van Duyne, R. P. *J. Phys. Chem. B* **2003**, *107*, 7426.
- (38) Draine, B. T.; Flatau, P. J. *User Guide for the Discrete Dipole Approximation Code DDSCAT.6.0*; <http://arxiv.org/ags.astro-ph/0309069>, 2003.